Superconductor Science and Technology

PAPER • **OPEN ACCESS**

A novel numerical approach for analyzing experimental data on critical current degradation in Nb_3Sn wires caused by transverse deformations preceding heat treatment

To cite this article: S Burioli *et al* 2024 *Supercond. Sci. Technol.* **37** 095007

OPEN ACCESS
IOP Publishing
Superconductor Science and Technology
Supercond. Sci. Technol. **37** (2024) 095007 (12pp)
https://doi.org/10.1088/1361-6668/ad68ac

A novel numerical approach for analyzing experimental data on critical current degradation in Nb_3Sn wires caused by transverse deformations preceding heat treatment

S Burioli[1,*], G Iannone[3], G De Marzi[3,5], D D'Agostino[3], G Avallone[3], A Gagno[1], M Bracco[1], A Leveratto[4], A Traverso[4], D Pedrini[2], R Valente[2], M Prioli[2], P Piccardo[6], A Malagoli[4], S Farinon[1] and R Musenich[1]

[1] INFN, Genoa, Italy
[2] LASA, INFN, Milan, Italy
[3] INFN, Salerno, Italy
[4] CNR/SPIN, Genoa, Italy
[5] ENEA, Frascati, Italy
[6] Chemistry, University of Genoa, Italy

E-mail: sergio.burioli@ge.infn.it

Received 2 April 2024, revised 18 June 2024
Accepted for publication 29 July 2024
Published 7 August 2024

Abstract

In the framework of studies on high-field magnets for future accelerators, a specific project called ASTRACT focuses on the effect of transverse strain on the critical current of Nb_3Sn wires. The first phase of the project addresses the effects of strain imposed on Nb_3Sn wires before heat treatment and the development of a procedure to directly compare critical current measurements with values extracted from magnetization cycles. A Nb_3Sn RRP-Ti wire was deformed to different values of transverse strain (10%, 15%, 20%, and 25%), and long samples were collected for transport measurements at 4.2 K, in a background field ranging from 10 to 14 T. Short samples were used for magnetization measurements (VSM technique). Additionally, SEM images of the cross-section were collected at different longitudinal positions along the wire for each strain value. This paper proposes a method based on SEM image analysis and magnetization measurements analysis to study the effect of bundle deformation on transport properties. The procedure requires morphological information provided by SEM images after appropriate numerical processing. Verification through statistical comparison between the Ic transport and VSM data is also conducted. Direct critical current measurements showed no

* Author to whom any correspondence should be addressed.

degradation due to deformation up to 25%. The method introduced, independent of transport data, can reach the same conclusions by considering the real shape of the bundles.

Keywords: Nb_3Sn wires, VSM, VAMAS, critical current, Bean model

1. Introduction

The future of the new high-energy physics (HEP) research program is heading towards very substantial projects. Notably, the future circular collider (FCC) and the muon collider stand out among these, necessitating a breakthrough in superconducting magnet technology. Specifically, for the FCC collider, a new generation of 16 T dipoles is required [1]. To achieve this goal, superconducting wires capable of carrying high current density ($J_c = 1500$ A mm^{-2} at 16 T and 4.2 K) are essential. Currently, the most promising candidates for winding the future dipoles and quadrupoles are cables made with Nb_3Sn wires [2]. This type of superconductor is highly brittle, and its critical current performance is dependent on strain and stress. Consequently, numerous experimental studies have been conducted to investigate the correlation between J_c and the internal stress/strain state of the wire [3, 4] and [5]. Moreover, the deformation that the wire undergone before the heat treatment (HT) can lead to the breackage of the diffusion barriers and to the merging of the filaments (bundles). Such severe deformations are common during the cabling process to produce the Rutherford cable [6].

In this context we aim to understand whether a transverse deformation applied to the wire before HT (pre-HT) can lead to a degradation of the critical current, even in the absence of barrier breakage, i.e. solely by changing the shape of the filament bundles. To address this question, we employ two experimental techniques to measure the critical current of deformed and undeformed wire samples: the direct transport technique [7] and the indirect evaluation based on magnetization measurements via vibrating sample magnetometer (VSM). The magnetization curves allows obtaining the critical current density $J_c(B)$ applying the Bean's model. In this framework the magnetic moment is given by $m(B) \propto J_c(B)F$, where F is a geometrical factor which depends on the distribution and shape of the bundles. In more detail, if we consider a superconducting bundle as a domain D in space, the definition of magnetic moment combined with the Bean's model allows us to write

$$\begin{aligned}\vec{m} &= \frac{1}{2}\int_D \vec{r}\wedge\vec{J}_c(B)\,\mathrm{d}v \\ &= \frac{1}{2}J_c(B)\int_D \vec{r}\wedge\hat{e}(\vec{r})\,\mathrm{d}v. \end{aligned} \quad (1)$$

In the second step, we assumed $\vec{J}_c = J_c(B)\hat{e}(\vec{r})$. Where the module $J_c(B)$ is independent of the position. Meanwhile, in general, the unit vector $\hat{e}(\vec{r})$ can change direction in space. In this way, we can factor out $J_c(B)$ from the integral. Therefore, evaluating the geometric factor F reduces to evaluating the integral itself. The analytical calculation is possible only in the case of simple geometries, see [8], neglecting the twist pitch and approximating the bundles as straight cylinders. In our approach, we aim to extend the evaluation of the integral in equation (1), maintaining the cylindrical bundle approximation, but considering its actual cross-section and thus its orientation relative to the applied external field.

The paper is structured as follows: in section 2, we introduce the samples and the experimental setups, along with a summary of the direct critical current measurement results that serve as our benchmark. Section 2.3 outlines the methods employed to extract J_c from the magnetometer data. We also present our method and, in section 3, we provide some considerations regarding the comparison between the I_c values obtained by the two methods. Section 4 is dedicated to presenting the results and discussions, and section 5 contains our conclusions.

2. Experimental data and methods

2.1. Samples

The Nb_3Sn wire we measured is a RRP-Ti 162/169 made by Bruker OST, and its main specifications are listed in table 1. In this paper, we present a comparison between two common experimental techniques used to measure the critical current: transport and magnetization measurements. These techniques require different sample dimensions. In the transport technique, approximately 1.3 meters of strand is wound around a TiAlV barrel [9], as shown in figure 1, using the same barrel for the HT and the measurement. In the VSM technique, the samples need to be shorter, approximately 5 mm in length, to fit within the uniform magnetic field region. During the HT, the wire extremities have to be clamped to prevent the leakage of liquid tin, but clamping a 5 mm long wire is not practicable. Therefore, we prepared wire segments longer than 50 mm clamped at the ends. After the HT we extracted a 5 mm section from the central part.

Since we are interested in the critical current degradation due to the deformation before the HT, we decided to roll the wire using the same mill in a single shot to ensure the best homogeneity of rolling. The transverse relative deformation is defined as $|d_0 - d_f|/d_0$. Where d_0 is the nominal diameter and d_f is the final diameter after the lamination. We chose nominal relative deformation values of 10%, 15%, 20%, and 25% (the samples will be hereafter identified as L10, L15, L20, L25, respectively), considering that the deformation range during Rutherford cabling, as reported in [6, 10] and [11], is from 10% to 40%. To focus on the effect of the bundle deformation avoiding the bundle merging we decided not to exceed 25% of

Table 1. Main specifications of the Nb_3Sn wire used in the production of our samples.

Nb_3Sn wire specs	
Diameter (mm)	1.0
Cu/non-Cu	0.9
I_c @ 4.2 K and 16 T (A)	560 ± 14
Sub-element nominal diam. (μm)	58
Filament twist pitch (mm)	19 ± 3
RRR, rolled	159 ± 14

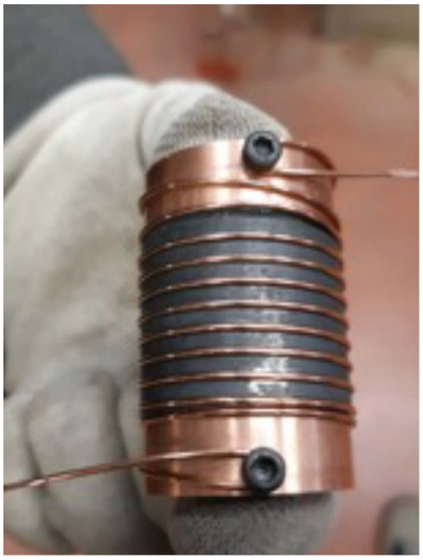

Figure 1. VAMAS barrel ready for the heat treatment.

Table 2. The table describes the sequence of plateaus in the heat treatment process. Each plateau is separated by a heating phase at $50\,^{\circ}\mathrm{C\,h^{-1}}$. At the end of the plateau at 665 °C, the cooling is natural.

Plateau temp (°C)	Duration (h)
210	48
400	48
665	72

rolling, since in the model we are proposing we assume that there are no interbundle currents.

The HT was performed following the recipe shown in table 2, with fluxing using Argon ($0.1\ \mathrm{Nlt\,min^{-1}}$). The last plateau was extended to 72 h, as suggested by the experience accumulated in the MQXFB series production.

The oven's thermally uniform region is approximately 500 mm long, enabling the HT of three barrels at time, along with the 50 mm VSM samples.

2.2. Transport measurements

The transport critical current measurements were conducted in a background solenoidal field ranging from 9 to 14 T at 4.2 K. Three VAMAS samples wound with virgin strand were measured, while only one VAMAS sample was measured for the L10, L15, and L25 samples. Unfortunately, the L20 VAMAS sample was lost possibly due to installation issues, and it was not possible to wind a new sample. The critical current from VAMAS samples was processed using the standard $V(I)$ relation

$$E = E_c \left(\frac{I}{I_c}\right)^n \tag{2}$$

with $E_c = 10\,\mu\mathrm{V\,m^{-1}}$. The voltage taps were soldered in the central part of the coil, 90 mm apart. In figure 2(a), we present a summary of the transport data, where the I_c is self-field corrected [12]. Regardless of the imposed deformation value, the I_c values are above the reference curve, which represents the $I_c(B)$ function using the parameters specified by the FCC collaboration requirements [2]. The figure 2(b) shows the critical current of deformed samples normalized to the average of the three virgin I_c, V1, V2 and V3 (defined as 100). If we align to the convention that 5% reduction is the threshold for critical current degradation, the plot shows no degradation at all until 25% of rolling.

As we will see in the following sections, transport data will be our primary estimator to validate the method introduced in this paper. Regarding the absence of the L20 VAMAS data, we decided to compare the VSM L20 I_c with the average critical current between the L15 and L25 VAMAS samples.

2.3. Magnetic measurement

In this section, we will describe the method for extracting critical current (I_c) values from the VSM data and outline the procedure for comparing them with the VAMAS I_c.

The magnetic moment curves were measured using a VSM made by Cryogenic Ltd in a background field up to 16 T. We measured a virgin sample extracted from the first virgin VAMAS sample. Its magnetic moment curve is depicted in figure 3. It is noteworthy that there are numerous flux jumps in the low field region, as expected in high-J_c Nb_3Sn wires. Concerning the rolled samples, we measured two samples, in the VSM, for any kind of rolling value.

2.3.1. I_c from VSM data: the analytical approach. As shown in the Introduction, we can derive J_c, and subsequently I_c, from the measurement of the magnetic moment. It has been demonstrated in [8] that if we approximate the bundles as hollow cylinders with an external radius R_o, internal radius R_i, longitudinal length $\mathcal{L}$, and we consider a linear superposition of N bundles (neglecting inter-bundle coupling currents), the equation (1) leads to

$$m = \frac{3}{4} J_c(B)\, \mathcal{L} N \left(R_o^3 - R_i^3\right). \tag{3}$$

While in the case of hollow cylindrical bundles with an elliptical cross-section, following the same approach of [8] in elliptical coordinates, our calculations lead to

$$m = \frac{3}{4} J_c(B)\, \mathcal{L} N \left(a_o b_o^2 - a_i b_i^2\right) \tag{4}$$

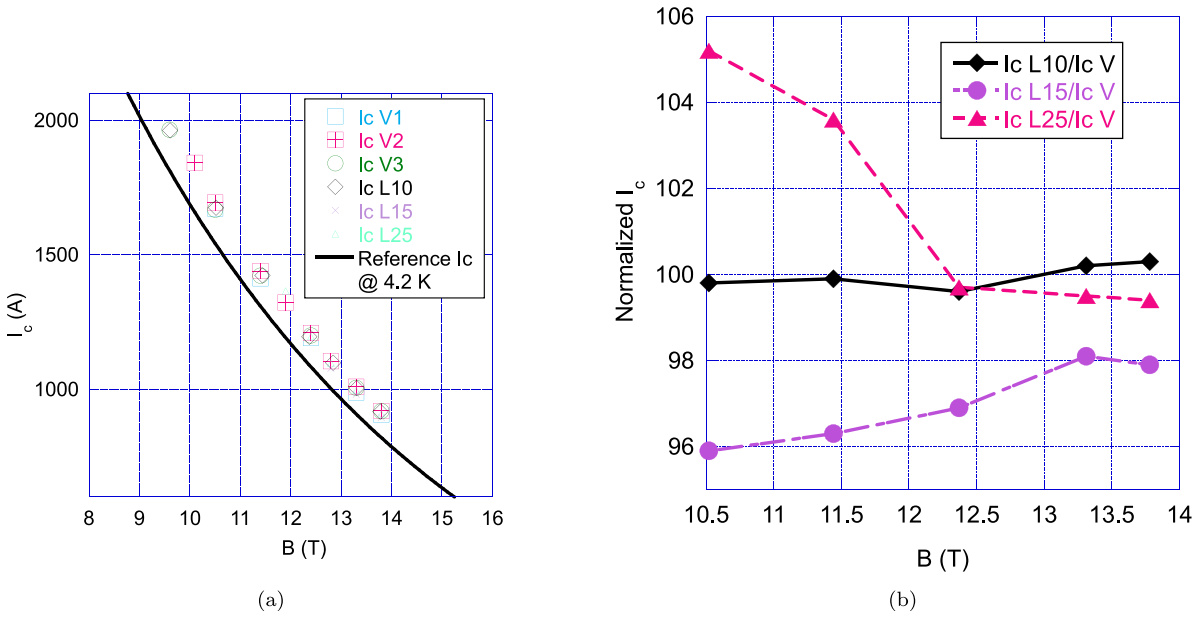

(a) (b)

Figure 2. A summary of transport data. On the left the Non-Cu critical current density compared to the reference $I_c(B)$ curve. On the right the normalized critical current from VAMAS data.

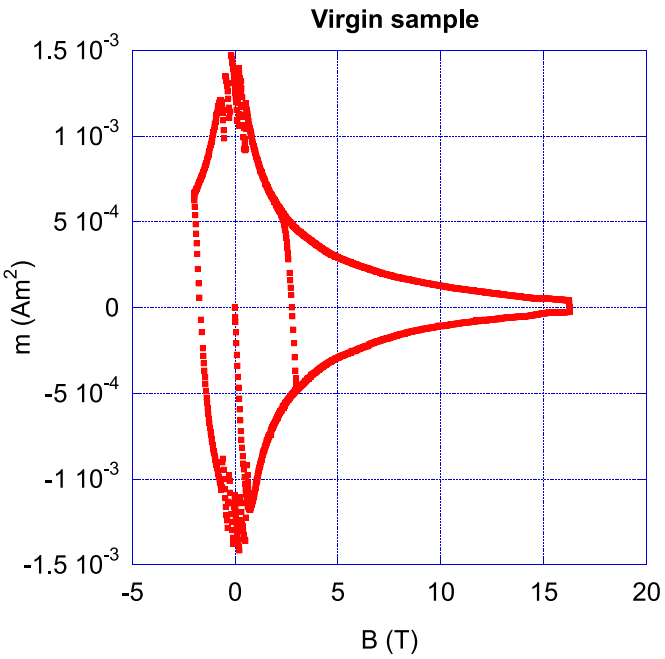

Figure 3. Magnetic moment of the sample extracted from a virgin VAMAS.

where a_i and a_o are the minor semi-axes of the inner and outer ellipses, while b_i and b_o are respectively the major semi-axes of the inner and outer ellipses (the major-axes perpendicular to the external field). The validity of equation (4) is limited to the cases of field parallel to the major or to the minor axis. For this reason, the elliptic bundle approximation is not used in this work for the analytical form factor evaluation. However, we report equation (4) because it will be used for a comparison of the analytical and numerical form factors in an ideal case.

To extract the J_c values this model requires geometrical information, specifically the sub-elements radii, from the SEM images. When applying this method to the $m(B)$ curve of figure 3 we get the results are shown in figure 4, where the empty circles represent the values obtained by the transport measurements just self-field corrected. Similarly to what highlighted in [8], we observe a systematic underestimation. It's important to note that the transport critical current values depend on the chosen electrical field criterion E_c. Since our purpose is also to improve the accuracy of the model presented in [8], we believe that the criterion used to define the critical current is an essential point for comparing the I_c from the two techniques. In the magnetic measurements the applied electric filed is related to $\mathrm{d}B/\mathrm{d}t$ and the sample geometry. Therefore, we decided to scale the critical currents given by the VAMAS data from the $10\,\mu\mathrm{V\,m^{-1}}$ criterion to an E_{VSM} defined in the next section.

2.3.2. The scaling procedure of the VAMAS data. Self-field corrections were applied to the VAMAS data. However, this correction alone is not sufficient to align with the transport data. Therefore, for a better comparison between VAMAS and VSM critical currents, we scale I_C^{VAMAS} from the $10\,\mu\mathrm{V\,m^{-1}}$ to a E_c^{VSM} criterion using the relation

$$I_c^L = I_c^{\mathrm{VAMAS};L}\left(\frac{E_c^{\mathrm{VSM}}}{10\,\mu\mathrm{V/m}}\right)^{\frac{1}{n}} \tag{5}$$

where $I_c^{\mathrm{VAMAS};L}$ is the critical current from VAMAS data self-field corrected and the suffix L means the lamination level. As reported in [13], the E_c^{VSM} can be estimated as the maximum electromotive force induced by the B field sweep rate divided by the superconducting screening current perimeter.

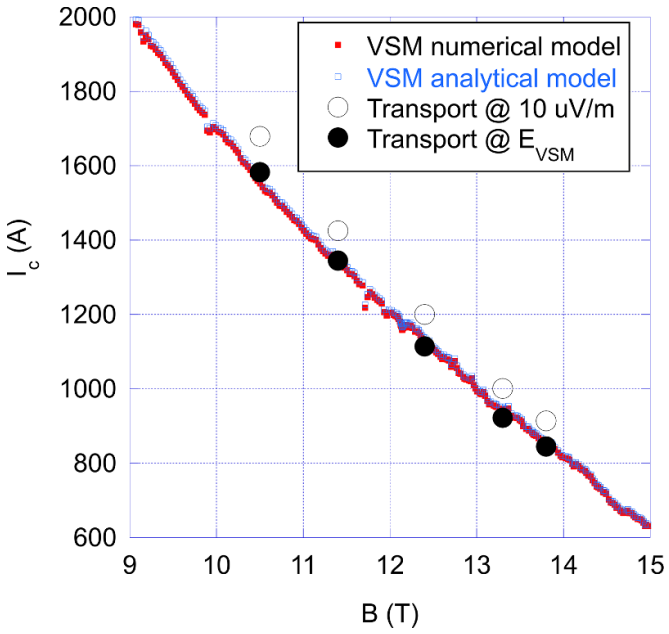

Figure 4. The plot displays the critical currents of the virgin sample using the $m(B)$ cycle from figure 3, processed using both the analytical and numerical shape factors, as described in section 2.3. The empty circles represent VAMAS data at $10\,\mu\mathrm{V\,m^{-1}}$, while the black circles are the same data scaled to a VSM electrical field.

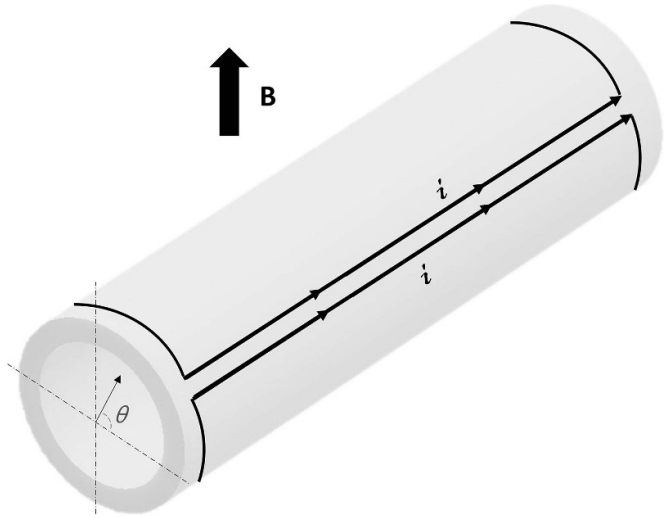

Figure 5. A sketch of the screening currents on a superconducting hollow cylinder.

In the case of a cylindrical bundle, the screening current flow is illustrated in figure 5.

The maximum induced electromotive force (e.m.f.) can be estimated by integration of $\dot{B}$ over the external upper surface at radius R_o

$$U = \int_0^{\pi} R_o \dot{B} \mathcal{L} \sin\theta \mathrm{d}\theta = 2\dot{B}\mathcal{L}R_o \tag{6}$$

where $\mathcal{L}$ is the longitudinal bundle length. So for the VSM we have

$$E_c^{VSM} = \frac{2\dot{B}\mathcal{L}R_o}{2\mathcal{L} + 2\pi R_o} \approx \dot{B}R_o \tag{7}$$

where R_o is in the order of tens μm and $\mathcal{L}$ is few mm. To extend equation (5) from a single bundle to a strand modeled as N straight cylindrical bundles, we introduce some additional assumptions to the previous Bean's model hypothesis. We assume that the bundles experience the same mean magnetic field B and temperature T, resulting in equal n-values and J_c values. Additionally, we approximate the bundles as hollow cylinders of constant external radius R_o. With these assumptions, we can state that during a I_c transport measurement, the current is evenly distributed among the sub-elements, leading to the expression

$$\begin{aligned} I_c^L &= \sum_{i=1}^{N} I_{c;i}^L \\ &= \sum_{i=1}^{N} \frac{I_c^{\mathrm{VAMAS};L}}{N} \left(\frac{\dot{B}R_{\mathrm{ext}}}{10\,\mu\mathrm{V/m}} \right)^{\frac{1}{n}} \\ &= I_c^{\mathrm{VAMAS};L} \left(\frac{\dot{B}R_{\mathrm{ext}}}{10\,\mu\mathrm{V/m}} \right)^{\frac{1}{n}}. \end{aligned} \tag{8}$$

In our data analysis R_o has been replaced with $\hat{R}_o$, see equation (14), averaged over any set of SEM pictures as reported in table 4.

Referring to the example depicted in figure 4, the scaling procedure emerges as a valuable tool in enhancing the concordance between VSM and VAMAS critical current assessments. However, when subjecting the wire to a transverse deformation, the bundles undergo alterations in their shape, loosing their quasi-circular symmetry. Herein lies the need to account for bundle deformation and its orientation to the external field in the evaluation of the geometrical factor F. Consequently, the following sections introduce a numerical approach aimed at further augmenting the model's accuracy, especially applicable to rolled samples.

2.3.3. SEM images. In our method, SEM images serve as a source of information about the geometrical properties of bundles, such as the internal and external mean radius. Since the bundles are not perfect circles but more akin to hexagons, our approach to extracting J_c from magnetic moment curves relies on the numerical evaluation of the proportional factor between $m(B)$ and $J_c(B)$, as depicted in the introduction. This approach allows us to consider the real bundle shape and their orientation in the background magnetic field inside the VSM. For each rolling value and the virgin sample, we acquired SEM images of the transverse section. The SEM used is a Zeiss Evo40 with an image pixel size of approximately 737.8 nm. Figure 6 provides an overview of the pictures, highlighting the merging of bundles in the 20% and 25% cases. In these latter two cases (see figures 6(d) and

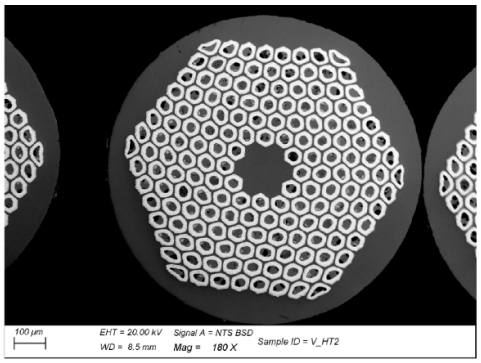

(a) *Virgin sample*

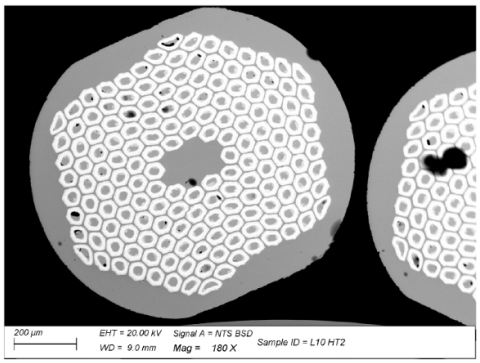

(b) *10% of rolling*

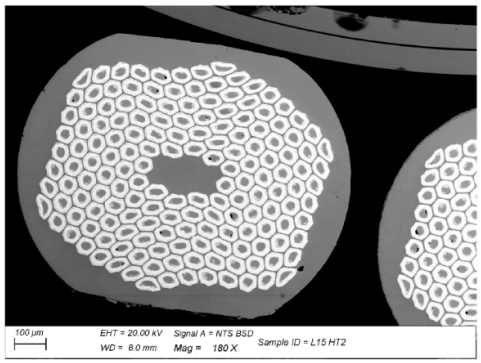

(c) *15% of rolling*

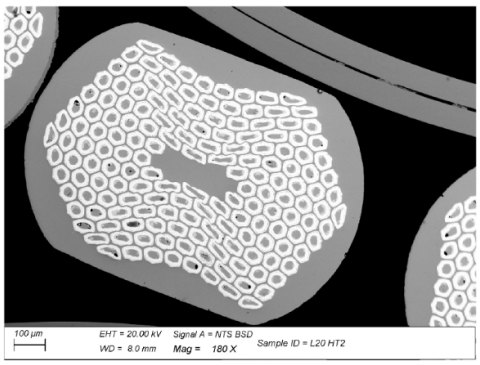

(d) *20% of rolling*

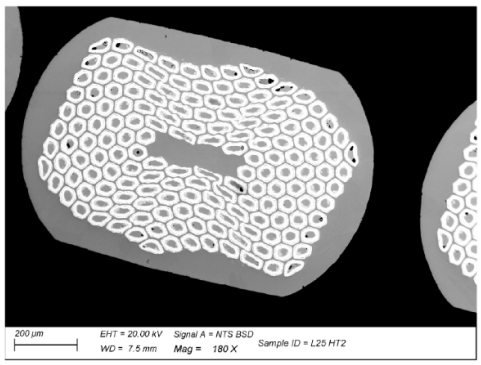

(e) *25% of rolling*

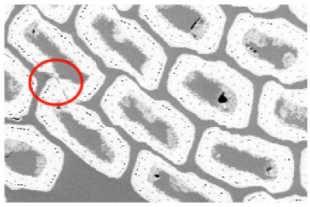

(f) *20% of rolling: zoom on merged bundles*

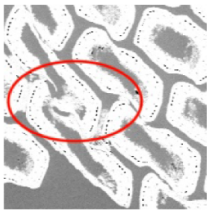

(g) *25% of rolling: zoom on merged bundles*

(h) *25% of rolling: bundle removed during pre-processing*

Figure 6. SEM images examples with zoom on L20 and L25 merged bundles.

(e)), some sub-elements are strongly deformed along the diagonal directions and around the center. Their contribution to the magnetic moment is primarily affected by the fact that they start to be very close to each other, merging in some cases, figures 6(f) and (g). Since our method is based on the hypothesis of no inter-bundle coupling currents, the presence of merged bundles is a clear deviation from this assumption. We looked for a way to address this singularity in our model and ultimately decided to separate the merged bundles during the image pre-processing phase. We made this choice because

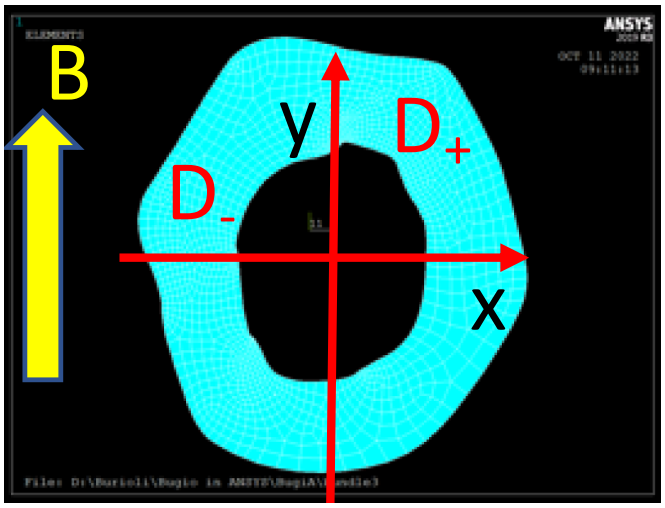

Figure 7. A sketch of the domain decomposition in our model. For convention, we choose to align the external magnetic field B parallel to the lateral side of the picture.

it represents the simplest way to apply our model in these cases, understanding that the final interpretation of the data analysis must take into account the physical implications of the merged bundles in the magnetic moment signal. There was only one case, involving an L25 image, where two bundles were merged and deformed excessively. In this situation, separation was not possible, and we decided to remove the bundle that resulted in a shape too deformed after pre-processing, as shown in figure 6(h). Losing one bundle out of 162 can be considered a minor statistical perturbation.

2.3.4. I_c from VSM data: the numerical approach. We decided to introduce a numerical evaluation of the integral in equation (1), based on a statistical sample of SEM images of the wire cross-section. Sampling SEM images at different positions along the wire, for any kind of lamination, is useful to average the effects of the bundle pitch.

Our model will be referred to as the 'numerical shape factor,' or F-model, to distinguish it from the analytical equation we have seen before. The starting point is the assumption that, in case of complete penetration, an external magnetic field separates the sub-element section into two domains, D_+ and D_-, spanning the same area

$$\int_{D_+} \mathrm{d}S = \int_{D_-} \mathrm{d}S. \tag{9}$$

This is illustrated in figure 7, and it is a consequence of the Bean's model and the law of current conservation.

So the integration domain in equation (1) is the Cartesian product of the cross-section of the bundle, as union of D_+ and D_-, and its longitudinal length: $D = (D_+ \cup D_-) \times [0, \mathcal{L}]$. Thus, given a bundle, we can find a straight line, parallel to B, that can split the bundle section in agreement with equation (9). Choosing a (x, y) coordinate system centered within the bundle, with unit vectors $\hat{i}$ and $\hat{j}$ and expanding the wedge product in the integral, we have

$$\int_D \vec{r} \wedge \vec{e}_z(\vec{r})\, \mathrm{d}^3 r = \mathcal{L}\left[\hat{i}\left(\int_{D_+} y\mathrm{d}x\mathrm{d}y - \int_{D_-} y\mathrm{d}x\mathrm{d}y\right) + \hat{j}\left(\int_{D_-} x\mathrm{d}x\mathrm{d}y - \int_{D_+} x\mathrm{d}x\mathrm{d}y\right)\right]. \tag{10}$$

To simplify our code, we assume the external B field to be parallel to the y-axis, as the field orientation can be arbitrary, and we will rotate the image to fulfill the experimental conditions. For each bundle, we calculate the center of mass and perform a coordinate translation to it. In this local coordinate system, to find the domains D_+ and D_- we run an algorithm shifting the y-axis until condition expressed by equation (9) is fulfilled up to a certain cutoff value $(2 \cdot 10^{-12}, \mathrm{m}^2)$. Then, the integral in equation (10) is numerically evaluated. This code has been implemented in ANSYS mainly for two reasons. First, thanks to the SpaceClaim ANSYS program, the JPEG images can be easily imported into ANSYS APDL via the ANSYS Neutral Format (see figures 8(b) and (d)). As a result, each bundle becomes a surface that we can mesh using PLANE183 elements, leading to an approximated evaluation of equation (1) in the form

$$\vec{m}_{\mathrm{bundle}} \approx J_C \mathcal{L}\left[\hat{i}\left(\sum_{i=1}^{N_+} y_C^i \delta S_i - \sum_{i=1}^{N_-} y_C^i \delta S_i\right) + \hat{j}\left(\sum_{i=1}^{N_-} x_C^i \delta S_i - \sum_{i=1}^{N_+} x_C^i \delta S_i\right)\right]. \tag{11}$$

In this equation, N_+ and N_- represent the number of elements in D_+ and D_-; (x_C^i, y_C^i) are the centroid coordinates of the ith element, and δS_i is its area. Since we are modeling with a 2D geometry where the current loops are infinitely long, according to [14] and [15], the factor $1/2$ must be omitted from equation (1). Additionally, the VSM measures the magnetic moment component parallel to the external magnetic field, so we can ignore the $\hat{i}$ components. Finally, our definition of the numerical shape factor of a single bundle becomes

$$F_{\mathrm{bundle}} = \sum_{i=1}^{N_-} x_C^i \delta S_i - \sum_{i=1}^{N_+} x_C^i \delta S_i. \tag{12}$$

As a second feature, APDL coding permits very easy rotation of the entire section since, for rolled samples, the flat side of the copper matrix has to be parallel to the external field. This requirement corresponds to the natural position in the VSM sample-holder and is very important for the shape factor evaluation of deformed samples. We can calculate the critical current from a magnetization curve as

$$I_c^{\mathrm{VSM};L} = \frac{m_{\mathrm{irr}}}{\mathcal{L}F} S_{\mathrm{SC}} \tag{13}$$

where the suffix L means the lamination level (V for virgin sample, 10% for 10% and so on); $m_{\mathrm{irr}} = |m_+(B) - m_-(B)|/2$

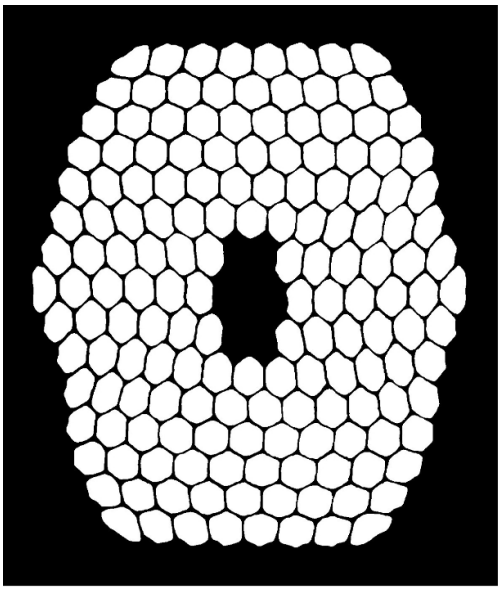

(a) *NonCu B&W example for a L15 section (jpeg format).*

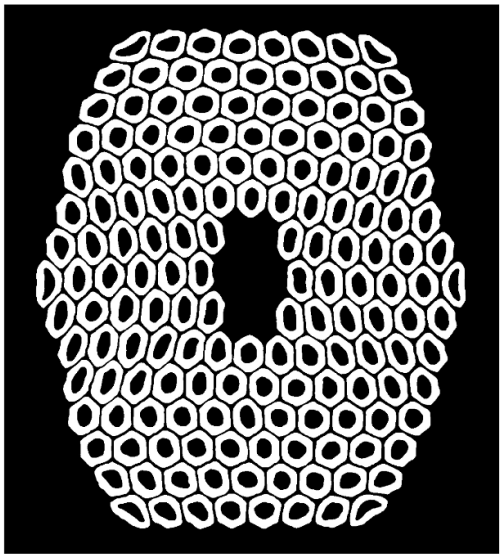

(b) *Effective SC section B&W example for a L15 sample (jpeg format).*

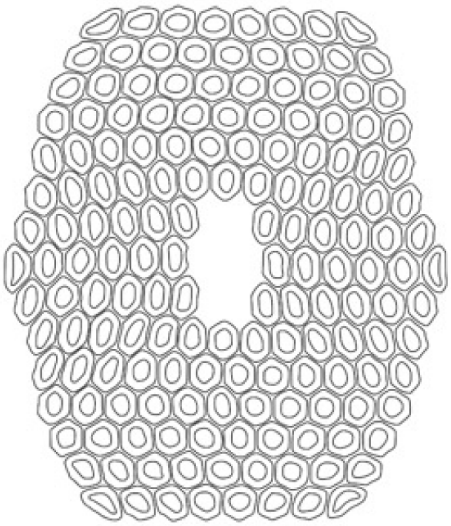

(c) *The image imported in SpaceClaim thanks to a conversion from jpeg to DXF.*

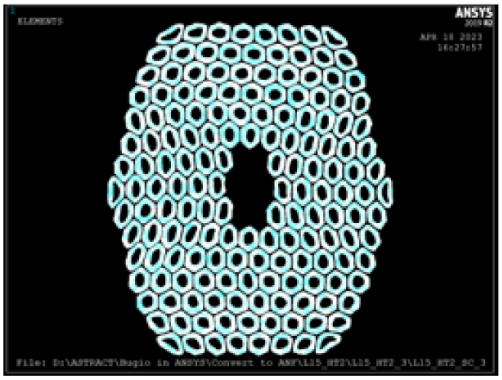

(d) *Final importation in ANSYS APDL via Ansys Neutral Format file by SpaceClaim.*

Figure 8. An example of the pre-processing elaboration for an L15 SEM image is shown in the figure. GIMP has been used for the effective superconducting surface S_{SC}, while ImageJ has been used for the NonCu case.

is the irreversible magnetic moment of the sample, measured parallel to a magnetic external field perpendicular to the wire, it is calculated as the semi-difference between the upper and lower branch of the magnetization curve; $\mathcal{L}$ is the sample lenght (mm); F is the total shape factor, i.e. equation (12) summed over all the bundles; S_{SC} is the effective total superconducting section. This last parameter can be evaluated by running the same ANSYS code on every SEM image. Additionally, the code can measure the total non-copper area, S_{NonCu}. Together, they give us the core total area as $S_{\mathrm{core}} = S_{\mathrm{NonCu}} - S_{\mathrm{SC}}$. Finally, the inner and outer radius can be defined as

$$\hat{R}_o = \sqrt{\frac{S_{\mathrm{NonCu}}}{\pi N}} \quad \text{and} \quad \hat{R}_i = \sqrt{\frac{S_{\mathrm{Core}}}{\pi N}} \tag{14}$$

where N is the number of subelements, see table 4. With this data, we can calculate the total analytical shape factor f, using equation (3), for any SEM image.

In order to compare the analytical and numerical shape factors, we calculated them in the ideal cases of perfect circular and elliptical bundles. The values and their relative difference are reported in table 3. The agreement is good, with differences around tens of parts per million (ppm). Since there is no formula to validate the method against for a real-shaped bundle,

Table 3. The shape factor evaluation for perfect bundles: theoretical value f vs numerical value F. $R_o = 29.6\,\mu$m; $R_i = 18\,\mu$m; $b_o = R_o$; $b_i = R_i$; $a_o = 26.2\,\mu$m; $a_i = 13.8\,\mu$m.

Perfect bundle	$f(\mathrm{m}^3)$	F from ANSYS code (m^3)	$\lvert f-F\rvert/f$
Circular $f = 4/3(R_o^3 - R_i^3)$	$2.6803\,10^{-14}$	$2.6802\,10^{-14}$	$50\ 10^{-6}$
Elliptic $f = 4/3(a_o b_o^2 - a_i b_i^2)$	$2.4646\,10^{-14}$	$2.4646\,10^{-14}$	$14\ 10^{-6}$

we aim to establish a benchmark for our model. To achieve this, we compare the numerical and analytical shape factors calculated from the SEM images of virgin samples. Table 4 presents the relative difference between F and f, with values representing the average over their respective image sets. In the case of virgin samples, the relative error is less than 1%, which is expected since the circular approximation is reasonably satisfied. However, as the lamination increases, the error grows almost linearly, and the F values consistently remain less than the f values.

3. Comparison between VAMAS and VSM data

The self-field corrections and the scaling procedure of the VAMAS data are necessary steps to compare transport and magnetization critical currents. Nevertheless we need a quantitative way to measure their compatibility. At this purpose we assume $I_c^{\mathrm{VAMAS};L}$, hereafter referred to more briefly as I_c^L, as best estimator and suppose the VSM $I_c^{\mathrm{VSM};L}$ to be a Gaussian observable centred in I_c^L, with standard deviation $\delta I_c^{\mathrm{VSM};L}$ estimated by the propagation errors applied to equation (13)

$$\frac{\delta I_c^{\mathrm{VSM};L}}{I_c^{\mathrm{VSM};L}} = \sqrt{\left(\frac{\delta m_{\mathrm{irr}}}{m_{\mathrm{irr}}}\right)^2 + \left(\frac{\delta l}{l}\right)^2 + \left(\frac{\delta F}{F} + \frac{\delta S_{\mathrm{SC}}}{\mathrm{SC}}\right)^2}. \quad (15)$$

The relative error in m_{irr} is about 1%; $\delta l/l$ is variable from 0.1% to 2%; $\delta F/F$ and $\delta S_{\mathrm{SC}}/S_{\mathrm{SC}}$ cannot be considered independent quantity since are derived from the same SEM image analysis. In addition, $\delta F/F$ varies between 1.1% and 2.4%. In our opinion, an error on F around one percent indicates a contained variability of the form factor in the longitudinal direction. The relative error in $I_c^{\mathrm{VSM};L}$ results in the range from 3% to 5%.

Our statistical approach is based on the parameter t, measuring the discrepancy respect to the standard deviation at a single B field value

$$t_L(B) = \frac{|I_c^{\mathrm{VSM};L}(B) - I_c^L(B)|}{\delta I_c^{\mathrm{VSM};L}(B)}. \quad (16)$$

Since VAMAS measurements correspond to a set of M points $(B_i, I_c^L(B_i))$, to summarize how the compatibility between $I_c^{\mathrm{VSM};L}$ and I_c^L is spread out over the B values, i.e. for a given L value, we look at average of t and its standard deviation σ_{t_L}. So we define

$$\bar{t}_L = 1/M \sum_i^M \frac{|I_c^{\mathrm{VSM};L}(B_i) - I_c^L(B_i)|}{\delta I_c^{\mathrm{VSM};L}(B_i)}. \quad (17)$$

From a global perspective, by defining $\bar{t}_L$, we aim to summarize the statistical compatibility of the data obtained at different external field values B. By selecting a mean compatibility criterion within 2 $\delta I_c^{\mathrm{VSM};L}$, the following conditions must be satisfied

$$\bar{t}_L \leqslant 1.0 \quad \text{and} \quad \sigma_{t_L} \leqslant 1.0. \quad (18)$$

We look also at the mean relative difference, i.e. the average along the B_i field values of the quantity

$$\mathrm{rel.diff}_L(B_i) = \frac{|I_c^{\mathrm{VSM};L}(B_i) - I_c^L(B_i)|}{I_c^L(B_i)}. \quad (19)$$

4. Results and discussion

The application of our model to the virgin sample is illustrated in figure 4. The analytical and numerical shape factors differ by approximately 0.6%. The statistical compatibility with the scaled transport data is less than one sigma (see table 5).

The results for the rolled samples VSM data are presented in figure 9. The red and blue curves represent the average critical current curves extracted from the m(B) cycle of two measured samples using the numerical and analytical methods, respectively. The empty circles correspond to VAMAS data corrected only for self-field, while the black dots are also scaled using equation (8). Compared to the virgin case, the red and blue curves consistently start to separate with significant deformation from the 15% rolling. For the L10%, L15%, and L20% samples, there is a strong agreement when employing our numerical model and the approach based on equation (8) to scale the transport data to the E_{VSM} criterion.

However, there is an exception in the case of L25. Its I_c^{VSM} appears to be improved by 7% more than the transport data, and there is no statistical compatibility, as shown in table 5. A global overview of the correlation between magnetic and transport critical current is presented in the plot of figure 10. It shows that all the VSM data, with the exception of L25, agree within 5% with their respective VAMAS counterparts.

We can use the previous definitions of section 3 to compare the analysis based on the numerical or analytical shape factors. We have to underling that this comparison is meaningful only if equation (17) is calculated respect to the scaled VAMAS data, also for the analytical model. The result is in table 5. According to the criterion indicated by equation (18) the two methods agree with the transport measurements until the 10% of rolling. In the case of L15 and L20, the analytical model is incompatible with the transport measurements. This means that, unlike the numerical model, the analytical one is

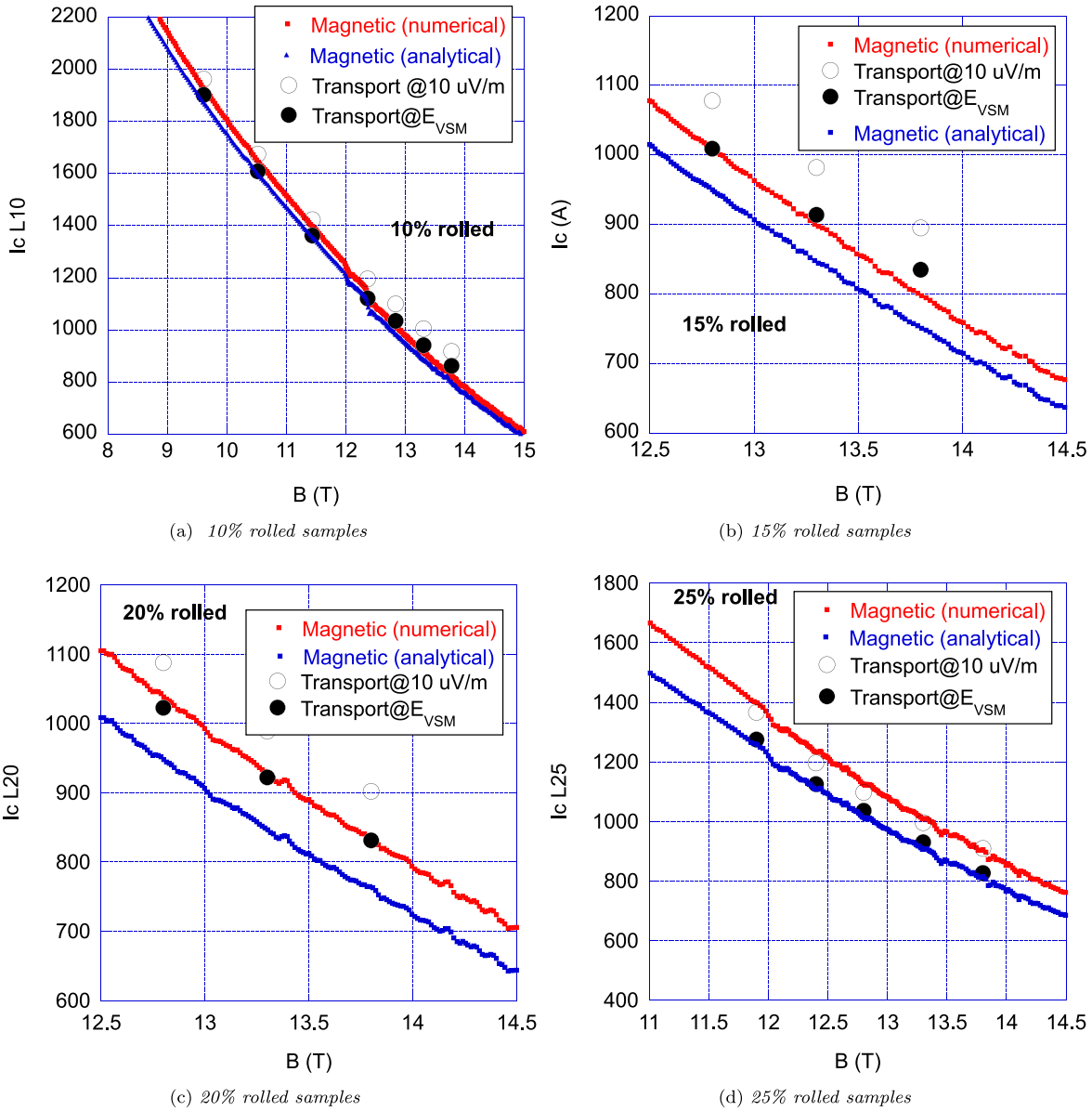

(a) *10% rolled samples* (b) *15% rolled samples*

(c) *20% rolled samples* (d) *25% rolled samples*

Figure 9. The plots summarize the results of the numerical (red) and analytical (blue) models used to extract I_c from the VSM data, compared to the critical current from the VAMAS measurements (empty circles are not scaled, i.e. $E_c = 10\,\mu\mathrm{V\,m^{-1}}$; black circles are scaled to E_{VSM}).

Table 4. The table shows the shape factor and the effective superconducting section evaluation for any kind of rolled sample. All values are averages calculated using the ANSYS code over a set of SEM images from the HT2 series. It also shows the analytical shape factor f by equation (3).

Sample	# SEM images	$< F >$ $(10^{-12}\,\mathrm{m^3})$	$< f >$ $(10^{-12}\,\mathrm{m^3})$	$\frac{\lvert<f>-<F>\rvert}{<f>}$ %	$< \hat{R}_o >$ μm	$< \hat{R}_i >$ μm	$< S_{\mathrm{SC}} >$ $(10^{-7}\,\mathrm{m^2})$	$< S_{\mathrm{NonCU}} >$ $(10^{-7}\,\mathrm{m^2})$
V_HT2	9	4.4947	4.4674	0.6	28.8	14.9	3.1016	4.2349
L10_HT2	4	4.6333	4.7735	3.0	29.4	14.8	3.2729	4.3989
L15_HT2	6	4.3576	4.6288	6.2	29.5	16.3	3.0890	4.4353
L20_HT2	6	3.8795	4.2510	9.6	28.8	16.1	2.8964	4.2187
L25_HT2	7	3.9097	4.3461	11.2	28.9	15.9	2.9621	4.2466

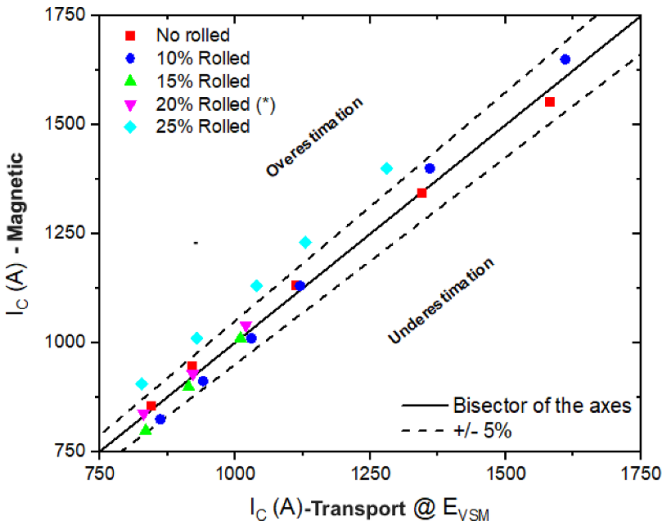

Figure 10. Correlation plot between magnetic, elaborated with the numerical shape factor, and transport critical current. The dashed lines delimit the ±5% maximum error region estimated with the errors propagation applied on equation (13).

Table 5. The table provides a comprehensive overview of the compatibility between the VSM critical currents and the VAMAS ones based on the quantities defined in section 3

Rolling%	Numerical model			Analytical model		
	$\bar{t}_L$	σ_{t_L}	$< \text{rel.diff}_L >$	$\bar{t}_L$	σ_{t_L}	$< \text{rel.diff}_L >$
0	0.6	0.4	0.6%	0.7	0.4	1.3%
10	0.7	0.4	−0.5%	1.0	0.8	−3.4%
15	0.5	0.5	−2.1%	1.9	0.5	−7.8%
20	0.4	0.3	1.6%	1.7	0.3	−7.3%
25	2.1	0.3	7.3%	0.9	0.2	−3.5%

unable to capture the differences due to the deformation of the bundles and their orientation with respect to the external magnetic field.

At 25% of lamination, there is an inversion such that the analytical model becomes highly compatible with the transport measurements, while the numerical model exceeds the 2σ on average. In our opinion, this paradox is a manifestation of the bundles merging which leads to lose the non-coupling current hypothesis over the 20% of rolling. This results in a stronger m_{irr} signal, as observed also in [16]. In the case of the analytical model, the more intense signal is offset by the shape factor, which remains more or less constant, see table 4. This causes the apparent compatibility with the transport measurements scaled to the criterion E_c^{VSM}. On the contrary, the interpretation made by the numerical model leads to an improved critical current, which is just an artifact, an indication of a threshold, above the 20% of rolling, that we cannot exceed, otherwise our method cannot be applied.

5. Conclusion

In this paper, we introduced a novel numerical method to estimate the critical current of Nb_3Sn wires from magnetic moment measurements. Our method involves numerically assessing the integral in equation (10), accounting for the effects of bundle shape deformation. We validated our approach by comparing the results with critical currents obtained by direct measurements on wires wound on VAMAS barrels. The comparison provided valuable insights into the role of the criterion applied to define the critical current, allowing us to determine a scaling procedure to align data obtained with the two methods. The comparison is fair if done between the values measured on wires that have undergone transverse deformations up 20%. Larger deformations lead to damage and merging of the bundles, therefore, even applying the numerical model and the correction to the critical current criterion, the values obtained from the magnetization measurements does not match that of the direct measurements. That is explained by the fact that the bundle merging invalidates one of the assumptions of the model, i.e. the absence of inter-bundle coupling currents. Level of deformation larger than 20% could be considered as a limit of the investigation of I_c through magnetic moment measurements.

Looking ahead, we aim to refine various aspects of our method to enhance its protocol and applicability, including geometrical information coming from 3D tomography.

Data availability statement

The data cannot be made publicly available upon publication because no suitable repository exists for hosting data in this

field of study. The data that support the findings of this study are available upon reasonable request from the authors.

Acknowledgments

The work is a collaboration among INFN, CNR-SPIN, ENEA and the Department of Chemestry, University of Genoa. It is funded by INFN CSN5 under the ASTRACT project.

The author extends sincere gratitude to Dr P Fabbricatore for invaluable discussions on critical aspects of the project. Special thanks are also due to Dr A Augeri from ENEA for his invaluable assistance during the VSM measurements campaign.

ORCID iDs

S Burioli https://orcid.org/0009-0008-9337-0049
G De Marzi https://orcid.org/0000-0002-5752-2315
A Leveratto https://orcid.org/0000-0001-8480-2884
A Traverso https://orcid.org/0000-0002-9690-2222
A Malagoli https://orcid.org/0000-0002-7204-9204
S Farinon https://orcid.org/0000-0002-6487-2137

References

[1] Schoerling D *et al* 2019 The 16 T dipole development program for FCC and HE-LHC *IEEE Trans. Appl. Supercond.* **29** 1–1
[2] Hopkins S 2019 *FCC Magnets Collaboration Meeting: Status of Conductor Procurement* (available at: https://indico.cern.ch/event/860937/contributions/3668944/)
[3] Gámperle L, Ferradas J, Barth C, Bordini B, Tommasini D and Senatore C 2020 Determination of the electromechanical limits of high-performance Nb_3Sn Rutherford cables under transverse stress from a single-wire experiment *Phys. Rev. Res.* **2** 013211
[4] Ekin J W 1987 Effect of transverse compressive stress on the critical current and upper critical field of Nb_3Sn *J. Appl. Phys.* **62** 4829–34
[5] Wang T, Chiesa L, Takayasu M and Bordini B 2014 Modeling of the critical-current behavior of Nb_3Sn subsized cables under transverse load using 2D finite element analysis and a strain scaling law *IEEE Trans. Appl. Supercond.* **24** 1–4
[6] Turrioni D, Barzi E, Bossert M, Collings E W, Nazareth V, Sumptions M D, Yamada R and Zlobin A V 2008 Effects of Rutherford cable parameters on Nb_3Sn extracted strand deformation and performance *IEEE Trans. Appl. Supercond.* **18** 1114–7
[7] 2006 Critical current measurement - DC critical current of Nb_3Sn composite superconductors *Technical Report* IEC 61788-2
[8] Baumgartner T, Eisterer M, Weber H W, Flükiger R, Bordini B, Bottura L and Scheuerlein C 2012 Evaluation of the critical current density of multifilamentary Nb_3Sn wires from magnetization measurements *IEEE Trans. Appl. Supercond.* **22** 6000604
[9] Wada H, Walters C R, Goodrich L F and Tachikawa K 1994 VAMAS intercomparison of critical current measurements on Nb_3Sn superconductors: a summary report *Cryogenics* **34** 899–908
[10] Rochepault E, Arbelaez D, Pong I and Dietderich D R 2015 Analysis and modeling of damage in RRP Nb_3Sn wires during cabling *IEEE Trans. Appl. Supercond.* **25** 1–5
[11] Zhang Y, Xu A, Dai C, Wu Y, Shi Y and Wu K 2020 Impact of transverse compression on the sub-element RRP Nb_3Sn strand *IEEE Trans. Appl. Supercond.* **30** 1–4
[12] Bordini B and Te-Msc 2010 (CERN) Self-field correction in critical current measurements of superconducting wires tested on ITER VAMAS barrels *Technical Report EDMS* nr. 1105765
[13] Eisterer M 2023 Magnetic measurements of critical current density, pinning and flux creep *Handbook of Superconductivity Characterization and Applications* vol 3 (CRC Press) p 881
[14] Brandt E H and Indenbom M 1993 Type-II-superconductor strip with current in a perpendicular magnetic field *Phys. Rev.* B **48** 12893–906
[15] Carr J W Jr 2001 *AC Loss and Macroscopic Theory of Superconductors* 2nd edn (CRC Press)
[16] Polyanskii A A, Lee P J, Jewell M C, Barzi E, Turrioni D, Zlobin A V and Larbalestier D C 2009 Evidence for highly localized damage in internal tin and powder-in-tube Nb_3Sn strands rolled before reaction obtained from coupled magneto-optical imaging and confocal laser scanning microscopy *Supercond. Sci. Technol.* **22** 095008